Dynamics of labyrinthine pattern formation in magnetic fluids

Stephen A. Langer
Department of Physics, Simon Fraser University, Burnaby, British Columbia, Canada V5A 1S6

Raymond E. Goldstein and David P. Jackson
Department of Physics, Joseph Henry Laboratories, Princeton University, Princeton, New Jersey 08544
(Received 23 April 1992)

A theory is developed for the dynamics of pattern formation in quasi-two-dimensional domains of magnetic fluids (ferrofluids) in transverse magnetic fields. The pattern formation is treated as a dissipative dynamical process, with the motion derived variationally from a static energy functional using minimal assumptions. This dynamics is one instance of a general formalism applicable to any system that can be modeled as a closed curve in a plane. In applying the formalism to ferrofluids, we present a calculation of the energy of a two-dimensional dipolar domain as a functional of the shape of its boundary. A detailed linear stability analysis of nearly circular shapes is presented, and pattern formation in the nonlinear regime, far from the onset of instability, is studied by numerical solution of the nonlinear, nonlocal evolution equations. The highly branched patterns obtained numerically bear a qualitative resemblance to those found experimentally. The time evolution exhibits sensitive dependence on initial conditions, suggesting the existence of many local minima in the space of accessible shapes. The analysis also provides a deterministic starting point for a theory of pattern formation in dipolar monolayers at the air-water interface, in which thermal fluctuations play a more dominant role.

PACS number(s): 68.10.−m, 68.70.+w, 75.70.Kw, 77.80.Dj

I. INTRODUCTION

Remarkable labyrinthine patterns are formed when a droplet of ferrofluid (a colloidal suspension of magnetic particles) is trapped between two horizontal glass plates in a vertical magnetic field [1]. These patterns, shown in Fig. 1, bear a strong resemblance to those found in solid-like monolayer domains of dipolar amphiphiles at the air-water interface [2–4]. This similarity reflects the common nature of the energetics of the two systems. Both are planar dipolar regions, with the dipoles perpendicularly aligned to the plane. Both are controlled by bulk dipole forces and line tension, and their motion is strongly overdamped. Viewed as pattern-forming systems, the only relevant degree of freedom in each is the shape of the boundary of the region, and as the pattern evolves this boundary is constrained by mass conservation to enclose a fixed area. An important distinction between the dynamics of these two systems is the importance of Brownian motion. The macroscopic magnetic fluid patterns obey an essentially deterministic dynamics, whereas the monolayer domains are on the scale of tens of micrometers, so that a full treatment of their dynamics would include a stochastic description of their large thermal fluctuations.

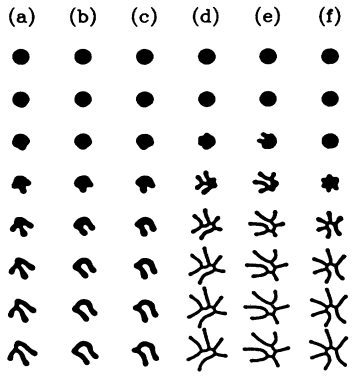

FIG. 1. Formation of branched ferrofluid patterns, from Ref. [12]. An initially circular droplet of ferrofluid in a Hele-Shaw cell (topmost figure in each column) is subjected to a perpendicular magnetic field. Time increases downward, the entire evolution taking approximately 30 sec. Columns (i)–(iii) are evolutions at low field (52 G), (iv)–(vi) at a higher field (63 G). The radius of the circular initial shape is 1.1 cm. Note the high degree of variability of the patterns starting from ostensibly identical conditions. For examples of fully developed labyrinths in various dipolar systems, see [1] and [3].

Other than aspects of the linear stability analysis of simple geometries [5,6], little is known theoretically about these complex shapes. Do the labyrinthine patterns actually minimize the energy of the electromagnetic and surface interactions, or are they the result of complicated hydrodynamic effects [7]? If the former, are the patterns unique ground states, or, like glasses, only local minima in a tortuous energy landscape?

In this paper, we address these questions by developing a formalism for the description of the dissipative motion of closed curves, conserving area, and derived variationally from a general energy functional. In this perhaps simplest possible dynamics for a boundary, the hydrodynamics of the surrounding medium is ignored except to the extent that it provides dissipation. The formalism thus resembles the time-dependent Ginzburg-Landau model familiar from the dynamics of phase transitions [8]. To apply the method to ferrofluids and monolayers,

in Sec. II we express the bulk dipolar energy of a finite domain as a functional of its boundary, a closed curve [9]. Through the formalism developed in Sec. III we arrive at a nonlinear nonlocal partial differential equation for the boundary's evolution. As a first step towards understanding the pattern formation in the dipolar systems, in Sec. IV we use the model to study the time evolution of a single domain prepared in an unstable state. Such a situation arises experimentally when the field on a ferrofluid [12] or the temperature or pressure of an amphiphilic film is suddenly changed [4]. A natural starting point for such a study is the linear stability analysis for a circular droplet. Computing the growth rates of small harmonic perturbations allows us to find the most unstable wavelength as a function of the control parameters. While in many pattern-forming systems (e.g., the Rayleigh-Bénard [10] and Mullins-Sekerka [11] problems) the most unstable wavelength is close to the spatial scale of the observed pattern in the nonlinear regime, this does not appear to be the case here, as we demonstrate with numerical studies far away from the region of validity of the linear analysis. The linear analysis does, however, reveal the essential physics of the instability: a competition between, on the one hand, fringe-field effects leading to a negative contribution to the line tension, and, on the other hand, long-range interactions between different parts of the boundary. It also provides a rough estimate of the number of arms of the labyrinth.

Our results may be summarized by the time-evolution sequences shown in Fig. 2, obtained from the nonlinear numerical calculations. These patterns display many of the features seen in experiment, including the qualitative features of the branching and the well-defined arm width. On a more conceptual level, these results suggest that in these systems a complex "energy landscape" can arise from simple rules involving only constraints and long-range forces. Consistent with this picture, the detailed final states of the pattern evolution display sensitive dependence on initial conditions, a phenomenon seen in experiment [12].

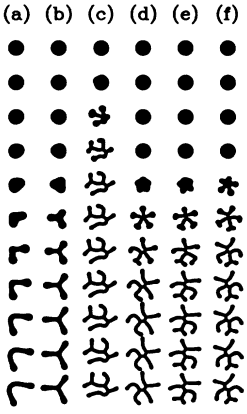

FIG. 2. Theoretical pattern evolutions for a dipolar domain, obtained from the numerical solution of the dynamical equations. Time increases downwards. Each column has microscopically different initial conditions, but (a) and (b) have the same control parameters ($N_{Bo}=1.01, p=20.0$) as do (c)–(f) ($N_{Bo}=0.54, p=200.$) See text for definition of N_{Bo} and p.

II. ENERGETICS OF DIPOLAR DOMAINS

The energy of a dipolar domain is taken to be the sum of electrostatic (or magnetostatic) and surface energies. We are considering domains of fixed area, so the relevant surface energy is due to the line tension γ around the boundary of the domain. In other words, the energy is

$$\mathcal{E}_0=\gamma L+\mathcal{E}_f\ , \tag{2.1}$$

where L is the length of boundary, and $\mathcal{E}_f$ is the dipolar energy, calculated as follows.

Consider a slab of thickness h in the $\hat{\mathbf{z}}$ direction and with a uniform cross section described by an arbitrary simple closed curve $\mathcal{C}$ in the xy plane (see Fig. 3). If this region is filled with a uniform density of dipoles oriented in the $\hat{\mathbf{z}}$ direction, then the field due to the dipoles is equivalent to that of two planar sheets of equal and opposite charge density σ, bounded by $\mathcal{C}$, and separated by h. Following Keller, Korb, and McConnell [13], we write the total field as $\mathbf{E}=\mathbf{E}_0+\mathbf{E}_1$, where $\mathbf{E}_0(x,y,z)$ is a uniform field $E_0\hat{\mathbf{z}}$ between the sheets [i.e., for $0\le z\le h$ and (x,y) within $\mathcal{C}$] and vanishes elsewhere. The corrections (not necessarily small) due to fringing are all contained in $\mathbf{E}_1$. Setting $E_0=4\pi\sigma$ means that, by Gauss' law, $\mathbf{E}_1$ is divergenceless. For convenience, we take E_0, rather than σ, to be the independent variable. In the magnetostatic problem, $E_0/4\pi$ corresponds to the magnetization M_0 of the ferrofluid.

Because $\mathbf{E}_1$ is divergenceless, we can define a vector potential $\mathbf{A}$ such that $\mathbf{E}_1=\nabla\times\mathbf{A}$. With $\nabla\cdot\mathbf{A}=0$, and observing that $\nabla\times\mathbf{E}_1=-\nabla\times\mathbf{E}_0$ is nonzero only on the ribbon-shaped boundary of the slab, we find

$$\mathbf{A}(\mathbf{x})=-\frac{E_0}{4\pi}\int_0^h dz'\oint_{\mathcal{C}} ds'\frac{\hat{\mathbf{t}}(s')}{|\mathbf{x}-\mathbf{r}(s',z')|}\ , \tag{2.2}$$

where $\mathbf{x}$ is any point is space, s' is an arclength coordi-

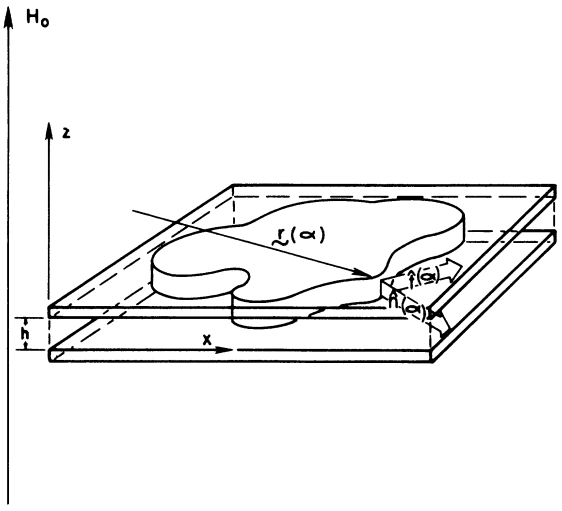

FIG. 3. Schematic illustration of the slab geometry of a ferrofluid experiment, with definitions of the geometric quantities describing the curve $\mathcal{C}$.

nate along the contour $\mathcal{C}$, $\mathbf{r}(s',z')$ is a point on the ribbon, and $\hat{\mathbf{t}}(s')$ is the unit counterclockwise tangent to $\mathcal{C}$ at s'. $\mathbf{A}$ is identical to the vector potential produced by a ribbon of current flowing around the boundary of the slab, with a density $E_0 c/4\pi$ per unit height.

The field energy is

$$\mathcal{E}_f=\frac{1}{8\pi}\int d^3r(|\mathbf{E}_0|^2+2\mathbf{E}_0\cdot\mathbf{E}_1+|\mathbf{E}_1|^2)\ . \tag{2.3}$$

The first term, arising from the uniform field, is simply proportional to the volume of the slab. The cross term is nonzero only within the slab. Using Eq. (2.2) and Stokes' law, we can reduce this term to a double integral over the ribbon bounding the slab:

$$2\int d^3r\mathbf{E}_0\cdot\mathbf{E}_1=-\frac{E_0^2}{2\pi}\int\int_0^h dz\,dz'\oint ds\oint ds'\frac{\hat{\mathbf{t}}\cdot\hat{\mathbf{t}}'}{|\mathbf{r}-\mathbf{r}'|}\ . \tag{2.4}$$

Here the primed and unprimed variables indicate quantities evaluated at the primed and unprimed coordinates (s',z') and (s,z). Note that this term is negative, reflecting the fact that the fringe field $\mathbf{E}_1$ opposes the bulk field $\mathbf{E}_0$ at the boundary. Later we shall see that this has the effect of decreasing the effective line tension of the boundary, thus favoring an increase in the perimeter.

The last term in (2.3) is simplified by noting that, by the divergence theorem [14], $\int d^3r|\mathbf{E}_1|^2 \equiv\int d^3r(\nabla\times\mathbf{A})\cdot\mathbf{E}_1=\int d^3r\,\mathbf{A}\cdot(\nabla\times\mathbf{E}_1)$, which finally reduces to an integral over the ribbon. In the end, this term is exactly $-\frac{1}{2}$ of the cross term (2.4).

Writing $|\mathbf{r}-\mathbf{r}'|=\sqrt{R^2+(z-z')^2}$, where $R=|\mathbf{R}| =|\mathbf{r}(s')-\mathbf{r}(s)|$ is the *in-plane* distance between points at positions s and s' on $\mathcal{C}$, lets us perform the integrals over z and z' analytically, and we can express the full field energy as a functional of a self-interacting closed curve in the plane:

$$\mathcal{E}_f=\frac{hE_0^2}{8\pi}\left\{\mathcal{A}-\frac{1}{2\pi}\oint ds\oint ds\,\hat{\mathbf{t}}\cdot\hat{\mathbf{t}}'\Phi(R/h)\right\}\ , \tag{2.5}$$

with

$$\Phi(\xi)=\sinh^{-1}(1/\xi)+\xi-\sqrt{1+\xi^2}\ . \tag{2.6}$$

Figure 4 illustrates that for $\xi\gg1$, the function Φ is essentially Coulombic ($\Phi\simeq1/2\xi$), whereas for $\xi\leq1$ it is less singular, varying as $\ln(2/\xi)$. This crossover to logarithmic behavior occurs because of the finite thickness h of the slab, and prevents the integrals from diverging. Earlier studies [13,15,16], in which the integrals over z and z' in Eq. (2.4) were absent, required an additional small scale cutoff. We stress that the result (2.5) is an exact representation of the field energy, within the approximation of a uniform dipolar density. By taking the limit $h\to0$ in (2.5), one can recover the expression in [13], but only for the range where $R\gg h$ in the integrand.

Defining a dipole moment density $\mu=\sigma h$ (per unit area), we have $E_0=4\pi\mu/h$. Written this way, the correspondence with magnetic systems is simply $\sigma\to M_0$, or $\mu\to M_0 h$, where M_0 is the assumed uniform magnetization. Rescaling all lengths by the height h, we see that the full energy (2.1) is determined by one dimensionless parameter, the "magnetic Bond number" [1]

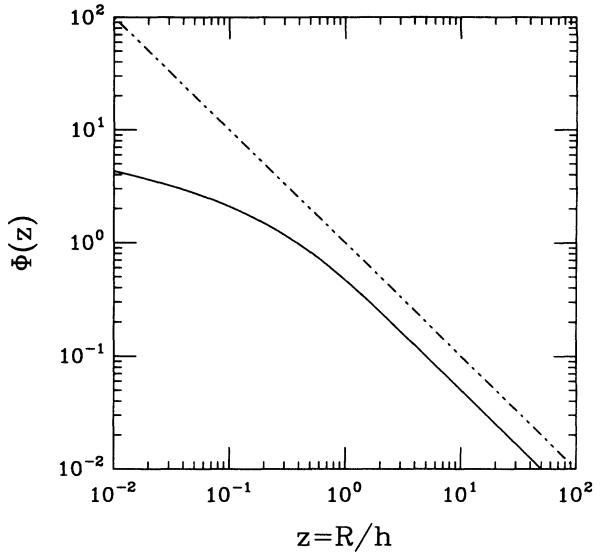

FIG. 4. Scalar potential Φ in Eq. (2.6) (solid line) compared with the Coulomb potential (dashed line).

$$N_{\rm bo}\equiv\frac{E_0^2h^2}{8\pi^2\gamma}=\frac{2M_0^2h^2}{\gamma} \tag{2.7}$$

and by the shape of the dipolar region. Because the enclosed area $\mathcal{A}$ will be unchanged by the dynamics, a convenient measure of the shape is the scaled aspect ratio

$$p\equiv2R_0/h\ , \tag{2.8}$$

where $R_0=\sqrt{\mathcal{A}/\pi}$ is the radius of the equivalent circle.

The importance of the logarithmic dependence of the pair potential Φ on the slab height can be seen through a computation of the energy of a circular disk, a result apparently first found by Lorenz [17]. An exercise in the manipulation of elliptic integrals yields

$$\mathcal{E}_f=\frac{E_0^2}{8\pi}\mathcal{A}h+\frac{E_0^2}{3\pi}R_0^3\{1-k^{-3}[(2k^2-1)E(k)+(1-k^2)K(k)]\}\ . \tag{2.9}$$

where K and E are, respectively, complete elliptic integrals of the first and second kind, and

$$k^2=\frac{p^2}{1+p^2}\ . \tag{2.10}$$

If we now consider the limit $h\to0$ while keeping the dipole density $\mu=E_0h$ fixed, the excess field energy diverges as

$$\mathcal{E}_f-\frac{E_0^2}{8\pi}\mathcal{A}h\simeq-2\pi\mu^2R_0\left\{\ln\left[\frac{8R_0}{e^{1/2}h}\right]+\mathcal{O}\left[\left[\frac{h}{R_0}\right]^2\ln\left[\frac{h}{R_0}\right]\right]\right\}\ , \tag{2.11}$$

illustrating the role of the height h as a cutoff.

III. DYNAMICS

A. A variational principle

Having reduced the energy of the dipolar domain to a functional of the curve $\mathcal{C}$, we now address the general problem of the motion of a closed curve in a plane. We will adopt the simplest possible dynamics, requiring no ingredients beyond those contained in the energy functional and the assumption of dissipation. We seek equations of motion for the curve that will always decrease its energy.

Let $\mathbf{r}(\alpha,t)$ be a closed curve, where $\alpha\in[0,1]$ is an arbitrary parametrization. It will often be convenient (as in the above discussion of the energy) to use the *arclength parametrization* $s(\alpha)$ of the curve, with differential $ds=\sqrt{g}\,d\alpha$, where $g\equiv|\partial\mathbf{r}/\partial\alpha|^2$ is the metric. If $\hat{\mathbf{n}}$ is the outward unit normal to the curve at α, and $\hat{\mathbf{t}}(\alpha)\equiv\partial\mathbf{r}/\partial s$ is the unit counterclockwise tangent, then $\partial\hat{\mathbf{n}}/\partial s=\kappa\hat{\mathbf{t}}$, and $\partial\hat{\mathbf{t}}/\partial s=-\kappa\hat{\mathbf{n}}$, where κ is the curvature, defined to be positive for a circle.

The equations of motion are derived from an action principle using Lagrange's formalism for dissipative processes [18,19]. This method guarantees that the resulting equations have the appropriate reparametrization invariance. The generalized coordinates q_α are the positions of the points $\mathbf{r}(\alpha)$ on the curve. The potential energy is simply the energy functional $\mathcal{E}[\mathbf{r}]$. In general, the equations of motion are

$$\frac{d}{dt}\frac{\partial\mathcal{L}}{\partial\dot{q}_\alpha}-\frac{\partial\mathcal{L}}{\partial q_\alpha}=-\frac{\partial\mathcal{F}_d}{\partial\dot{q}_\alpha}\ , \tag{3.1}$$

where $\mathcal{F}_d$ is the Rayleigh dissipation function, proportional to the rate at which energy is dissipated by the viscous forces.

For the typical viscous forces linear in the velocity, $\mathcal{F}_d$ is quadratic in $\partial\mathbf{r}/\partial t$. Making a local approximation, we write [20]

$$\mathcal{F}_d=\tfrac{1}{2}\eta\int_0^1 d\alpha\sqrt{g}\left|\frac{\partial\mathbf{r}}{\partial t}-\Theta(\alpha,t)\hat{\mathbf{t}}\right|^2\ , \tag{3.2}$$

where η is a friction coefficient. Since the motion must be invariant under arbitrary time-dependent reparametrizations, we need the "gauge function" $\Theta(\alpha,t)$ to ensure that the reparametrizations do not contribute to the dissipation. Under the transformation $\alpha\to\alpha'(\alpha,t)$, the velocity transforms as $\partial\mathbf{r}/\partial t\to\partial\mathbf{r}/\partial t+(\partial\mathbf{r}/\partial\alpha')(\partial\alpha'/\partial t)$, and the dissipation function is unchanged if we let $\Theta\to\Theta+\sqrt{g}\,\partial\alpha'/\partial t$.

In the viscous limit we neglect the kinetic-energy terms in (3.1), setting $\mathcal{L}=-\mathcal{E}$. Then, recognizing that derivatives with respect to the coordinate q_α are functional derivatives with respect to $\mathbf{r}$, we obtain the equation of motion

$$\frac{\partial\mathbf{r}}{\partial t}=-\frac{1}{\sqrt{g}}\frac{\delta\mathcal{E}}{\delta\mathbf{r}}+\Theta\hat{\mathbf{t}}\ . \tag{3.3}$$

The friction coefficient η has been absorbed by rescaling time. The gauge function Θ appears as an additional tangential velocity, showing that it is indeed a reparametrization of the curve. Equation (3.3) has the appearance of the time-dependent Ginzburg-Landau equation for a nonconserved order parameter [8], and is also a generalized version of the Rouse model of polymer dynamics [21].

B. Kinematic constraints

Conservation of enclosed area is achieved through the introduction of a time-dependent pressure, Π, as a Lagrange multiplier in an augmented energy functional

$$\mathcal{E}=\mathcal{E}_0-\Pi\mathcal{A}\ . \tag{3.4}$$

$\mathcal{E}_0$ is the energy of the unconstrained system. To determine Π, we first define the normal and tangential velocities of a point on the curve:

$$\frac{\partial\mathbf{r}}{\partial t}=U(\alpha)\hat{\mathbf{n}}+W(\alpha)\hat{\mathbf{t}}\ . \tag{3.5}$$

We define two functions U_0 and W_0 to be the forces that are derived from $\mathcal{E}_0$ alone,

$$-\frac{1}{\sqrt{g}}\frac{\delta\mathcal{E}_0}{\delta\mathbf{r}}=U_0(\alpha,t)\hat{\mathbf{n}}+W_0(\alpha,t)\hat{\mathbf{t}}\ . \tag{3.6}$$

Functional differentiation of the augmented free energy (3.4), with $\mathcal{A}=(1/2)\oint ds\,\mathbf{r}\times\hat{\mathbf{t}}$ [22], yields dynamics in the form of (3.5) with

$$U(s)=U_0+\Pi\quad\text{and}\quad W(s)=W_0+\Theta\ . \tag{3.7}$$

Area conservation applied globally, $\partial\mathcal{A}/\partial t=0$, requires $\oint ds\,U(s)=0$. Thus Π is determined nonlocally at each instant of time to be

$$\Pi=-\frac{1}{L}\oint ds\,U_0\ . \tag{3.8}$$

It is worth remarking that although we assume that the dissipation function is local, the global area conservation constraint would introduce nonlocality into the dynamics even if the bare energy functional $\mathcal{E}_0$ were local.

C. Local arclength gauge and shape evolution

The constraint of fixed area manifests itself in the form of the normal velocity U, but leaves free the tangential velocity W, or equivalently, the reparametrization Θ in Eq. (3.7). We appeal to reparametrization invariance to choose a convenient tangential velocity W. For systems with conserved *total* arclength the natural choice would be one which preserves the meaning of arclength s by conserving the *local* arclength, i.e., the metric $\sqrt{g}$. When the total arclength is not constant, a useful choice is still that which maintains uniform spacing of points on the curve, the *relative arclength* gauge. The condition $(\partial/\partial t)(s/L)=0$ then requires that

$$W(s)=\frac{s}{L}\oint ds'\kappa U-\int_0^s ds'\kappa U\ . \tag{3.9}$$

For numerical work, rather than evolving a set of vectors $\{\mathbf{r}(\alpha)\}$, it is often convenient instead to follow the tangent angles $\{\Theta(\alpha)\}$ or the curvatures $\{\kappa(\alpha)\}$. These obey the equations [23]

$$\frac{\partial}{\partial t}\theta(\alpha,t)=-\frac{\partial U}{\partial s}+\kappa W \tag{3.10}$$

and

$$\frac{\partial}{\partial t}\kappa(\alpha,t)=-\left[\frac{\partial^2}{\partial s^2}+\kappa^2\right]U+\frac{\partial \kappa}{\partial s}W\ . \tag{3.11}$$

D. Example: Motion driven by line tension

To illustrate the formalism, we now discuss perhaps the simplest nontrivial example: a curve driven by line tension γ alone. The energy functional $\mathcal{E}_0=\gamma L$ is clearly minimized by shapes having the smallest possible perimeter consistent with the prescribed area, i.e., circles. The normal force is

$$U_0(s)=-\gamma\kappa \tag{3.12}$$

while the tangential force W_0 vanishes. Because $\oint ds\,\kappa=2\pi$ for a simple closed curve, Eq. (3.8) implies that the Lagrange multiplier is

$$\Pi=\frac{2\pi}{L}\gamma\ . \tag{3.13}$$

It follows that the final dynamics can be reduced to two coupled differential equations for the total length $L(t)$,

$$\frac{1}{\gamma}\frac{\partial L}{\partial t}=\frac{(2\pi)^2}{L}-\oint ds\,\kappa^2\ , \tag{3.14}$$

and for the curvature,

$$\begin{aligned}\frac{1}{\gamma}\frac{\partial\kappa(s,t)}{\partial t}=&\frac{\partial^2\kappa}{\partial s^2}+\kappa^3-\frac{2\pi}{L}\kappa^2\\&+\frac{\partial\kappa}{\partial s}\left[\frac{s}{L}\left[\frac{(2\pi)^2}{L}-\oint ds'\kappa^2\right]\right.\\&\left.-\left[\frac{2\pi}{L}\int_0^s ds'\kappa-\int_0^s ds'\kappa^2\right]\right]\ .\end{aligned} \tag{3.15}$$

Apart from the nonlocality associated with the reparametrizations, the dynamics in (3.15) is an area-conserving version of the well-studied "curve-shortening equation" [24]. A fixed point of these coupled equations is the circle $\kappa=1/R_0$ and $L=2\pi R_0$, where πR_0^2 is the area of the initial shape. The dynamics given by (3.14) and (3.15) will be discussed further in the next section as a description of shape relaxation of a labyrinthine pattern after the removal of the applied magnetic field.

IV. DYNAMICS OF DIPOLAR DOMAINS

A. Formulation

From the functional derivative of the full energy (2.1) and Eq. (3.6) we find the normal force at a point s on the boundary of a dipolar domain to be

$$U_0(s)=-\gamma\kappa+\frac{E_0^2}{8\pi^2}\oint ds'\hat{\mathbf{R}}\times\hat{\mathbf{t}}'[\sqrt{1+(h/R)^2}-1]\ , \tag{4.1}$$

where $\mathbf{R}=\mathbf{r}(s')-\mathbf{r}(s)$, $\hat{\mathbf{R}}=\mathbf{R}/R$ is the unit vector pointing from the point s towards s', and $R=|\mathbf{R}|$ is the distance between points s and s'. The tangential force $W_0(s)$ vanishes. The first term in (4.1) is the usual Laplace pressure due to the curvature of the interface. The second term, at large R, reduces to the Biot-Savart force due to a wire carrying an effective current $I=E_0hc/4\pi$ around the boundary. The deviation from the Biot-Savart form at small R results from the finite thickness of the effective wire, i.e., the height of the slab. Equation (4.1), together with (3.5) through (3.9), completely specifies the motion of the boundary. Note that the first term in the dipole energy (2.5) is proportional to the (conserved) slab volume, and does not contribute to the dynamics.

B. Linear stability analysis

When faced with complicated nonlinear dynamics problems, a fruitful approach is often to consider the linearized dynamics near a simple initial condition. For the ferrofluid, this analysis yields the critical magnetic field at which a circular droplet becomes unstable, and, given the field, the wavelength of the instability [25]. Because of the importance of nonlinearities in the dynamics and the finite width of the band of unstable modes, the wavelength of the initial instability does not necessarily uniquely determine the number of arms in the final labyrinth, although there is a strong correlation.

Consider small deviations ζ in the radius of a circle, parametrized by the polar angle φ:

$$\mathbf{r}(\varphi)=[R_0+\zeta(\varphi,t)]\hat{\mathbf{e}}_r(\varphi)\ . \tag{4.2}$$

It follows from the general dissipative equation of motion for the boundary of the system,

$$\frac{\partial\mathbf{r}}{\partial t}=(U_0+\Pi)\hat{\mathbf{n}}+\Theta\hat{\mathbf{t}}\ , \tag{4.3}$$

that the perturbation ζ will evolve according to the linearization of the normal velocity of the circle:

$$\frac{\partial}{\partial t}\zeta(\varphi,t)=U_0\{[R_0+\zeta(\varphi,t)]\hat{\mathbf{e}}_r\}-U_0(R_0\hat{\mathbf{e}}_r)\ . \tag{4.4}$$

The deviation of the pressure Π from its unperturbed value is quadratic in ζ and thus does not appear in the stability analysis. Tangential velocities also play no role at linear order, so we may choose the gauge function $\Theta=0$.

If we now suppose that the perturbation is of the form $\zeta(\varphi,t)\sim\exp(\sigma_n t)\cos n\varphi$, then by straightforward but lengthy algebra (see the Appendix) we find that the growth rate σ_n of mode n is given by

$$\left[\frac{R_0^2}{\gamma}\right]\sigma_n=(1-n^2)+N_{\mathrm{Bo}}\mathcal{D}_n(p)\ , \tag{4.5}$$

where

$$\begin{aligned}\mathcal{D}_n(p)=\frac{p^2}{2}\left[\sum_{j=1}^{n}\frac{2}{2j-1}+\int_0^{\pi/2}\frac{p\cos 2n\omega}{\Delta(\omega)}d\omega\right.\\\left.-2+k^{-1}[2E(k)+(k^2-2)K(k)]\right]\ .\end{aligned} \tag{4.6}$$

The parameters p and k are given by (2.8) and (2.10), and we have defined $\Delta(\omega)=\sqrt{1+p^2\sin^2(\omega)}$.

Note that σ_1 vanishes identically for all N_{Bo} since a perturbation of the form $\zeta_1\cos(\varphi)$ simply translates the curve rigidly, and the field and line tension contributions to the energy are of course invariant to such changes.

Figure 5 illustrates the behavior of the growth rate as the Bond number N_{Bo} is changed at fixed aspect ratio. In general, the $n=2$ mode is the first to become unstable. The boundary of limiting stability in the $p-N_{Bo}$ plane may be computed analytically from (4.5) and (4.6) (see the Appendix and Ref. [6]). This boundary is shown in Fig. 6, along with the lines along which each of the other modes n is at the maximum of σ_n. These lines thus define approximately the centers of the band in the $p-N_{Bo}$ plane within which a given mode dominates all others. We see, as remarked in earlier studies [13,16], that a circular drop may become unstable either by increasing the Bond number (increasing dipolar strength or reducing surface tension) or by growing larger (increasing p). Figure 6 is in some sense a putative "phase diagram" for the system—if nonlinearities were unimportant, one could predict from it the number of arms in a labyrinth given the bond number and aspect ratio. Note, however, that the width of the band of unstable modes becomes large quite rapidly with increasing bond number. Intuitively this would suggest the possibility of strong mode competition, and, indeed, as we will see below, as the labyrinth evolves it quickly leaves the domain of applicability of the linear stability analysis. At a fixed value of p, the most unstable mode is a rapidly increasing function of bond number, as shown in Fig. 7. The steplike behavior is due to the quantization of wavelengths around the circle.

In many experiments on magnetic fluid and dipole monolayer pattern formation the aspect ratio p is very large, with values of 20–100 being easily obtained for magnetic fluids, and of 10^3–10^4 for monolayers. One expects that the stability analysis should simplify considerably in this limit; indeed, the systematic expansion described in the Appendix yields the leading terms in the growth rate for large p and $n/p \ll 1$:

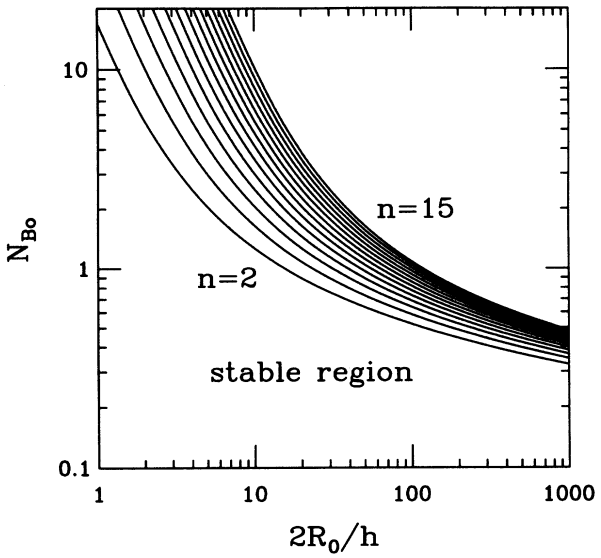

FIG. 6. Diagram illustrating dominant modes for instabilities of circular magnetic fluid domains. Bond number at which various modes have maximum growth rate, as a function of the aspect ratio $p=2R_0/h$. Equation (A11) was used to plot the line of initial instability (where the $n=2$ mode acquires a positive growth rate). The remaining curves were found by numerical solution of Eqs. (4.5) and (4.6) for extremal growth rates.

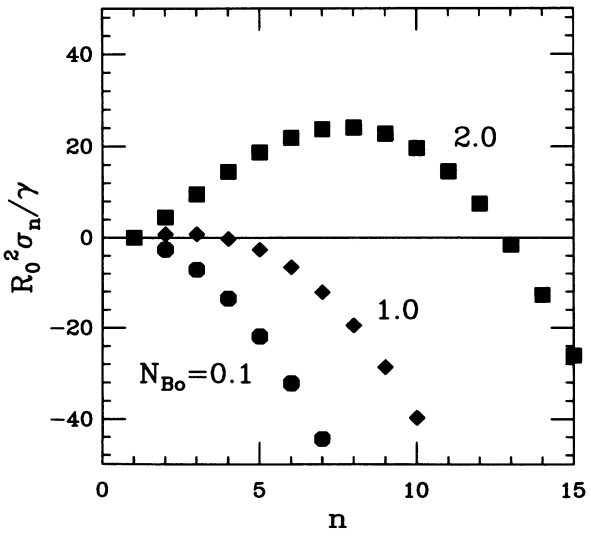

FIG. 5. Growth rate as a function of mode number in the linear stability analysis, for $p=20$ and three values of the magnetic Bond number.

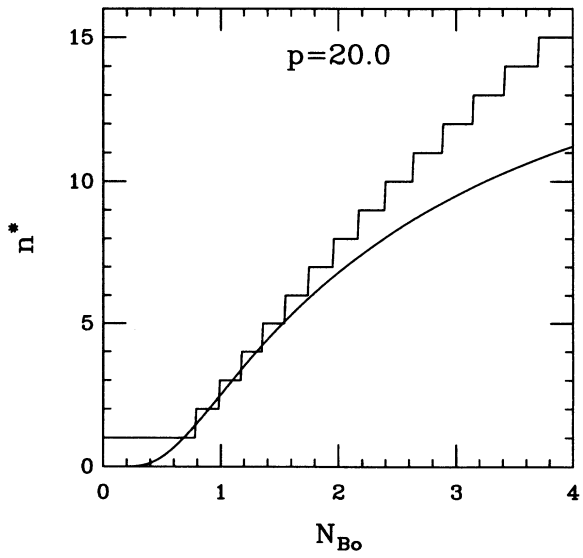

FIG. 7. Most unstable mode as a function of Bond number, for $p=20.0$. Stepped curve is from the exact linear stability analysis, illustrating the geometric locking due to the finite perimeter of the circle. Solid line is from the approximation (4.9).

$$\left[\frac{R_0^2}{\gamma}\right]\sigma_n = 1-n^2 + \tfrac{1}{2}N_{\mathrm{Bo}}\{(n^2-1)[1+\ln p - C]-n^2\ln n\}\ . \tag{4.7}$$

$C \simeq 0.577\,215$ is Euler's constant. We see that the magnetic interactions have two effects: (i) Terms in $(1-n^2)$ in (4.7) act like the line tension, so we find an effective line tension γ_{eff} in the presence of the magnetic field which is less than the bare tension, and can even be negative:

$$\gamma_{\mathrm{eff}} = \gamma[1-\tfrac{1}{2}(1+\ln p - C)N_{\mathrm{Bo}}]\ ; \tag{4.8}$$

(ii) the long-range magnetic forces between the parts of the interface introduce a logarithmic dependence on n (see the Appendix for details). For $n/p < 1$ this interaction is repulsive, destabilizing the circle.

A heuristic criterion for the onset of an instability might be developed simply by setting $\gamma_{\mathrm{eff}}=0$. From (4.8), this implies a critical value of the Bond number $N_{\mathrm{Bo}}=2/(1+\ln p - C)$, which is close to the instability line of the $n=2$ mode.

We deduce from (4.7) that the most unstable mode n^* has an extremely strong (and nonanalytic) dependence on the magnetic bond number,

$$n^* = \left[\frac{pe^{1/2}}{\gamma_E}\right]\exp(-2/N_{\mathrm{Bo}})\ , \tag{4.9}$$

as does the maximum n for which the growth rate is positive; i.e., the width of the band of unstable modes. Recast in terms of the most unstable wavelength, λ^*, we see the simple result that for large droplets λ^* is independent of the unperturbed radius R_0,

$$\lambda^* = \left[\frac{\pi\gamma_E}{e^{1/2}}\right]h\exp(2/N_{\mathrm{Bo}})\ , \tag{4.10}$$

as one would expect. As Fig. 7 illustrates, the large-p approximation to n^* is in reasonable qualitative and quantitative agreement with the exact result, particularly for $n/p \ll 1$.

C. Observed features in the nonlinear regime

Computational limitations restrict our studies to the early stages of labyrinth formation. We cannot reproduce numerically the highly convoluted labyrinths of Refs. [1] and [3]. However, the early labyrinth, with fewer than a dozen arms, is easily accessible, and is sufficient to indicate the mechanism of pattern formation. Figure 8 illustrates some numerical solutions of the dipolar dynamics for various values of the Bond number and aspect ratio. The dynamics reproduces several experimental features. The initially circular droplet evolves into a many-armed structure, with the number of arms increasing with the dipole density. The arms bend and branch, and have roughly constant width and bulbous ends. The droplets are not seen to break up. Note that while the mode number of the initial instability is in accord with the fastest growing mode n^*, obtained from the linear stability analysis (as summarized in the figure caption), subsequent branchings and mode competition result in a final number of arms which can differ from n^*. Moreover, as is apparent from the complex shapes, the actual length scales involved in the pattern have little to do with the wavelength of the initial instability, particularly since the total length is not conserved.

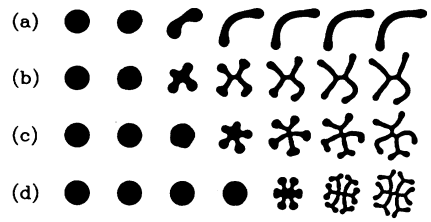

FIG. 8. Calculated time evolution for various values of the field-surface energy ratio N_{Bo} and initial aspect ratio p. The initial states are the nearly circular droplets at the left. Selected successive shapes are displaced horizontally for clarity. For each of the four conditions, the magnetic Bond number (N_{Bo}), aspect ratio (p), and the most unstable mode number (n^*) from the linear stability analysis, are (a) $N_{\mathrm{Bo}}=0.54$, $p=100$, $n^*=2$; (b) $n_{\mathrm{Bo}}=1.27$, $p=20$, $n^*=4$; (c) $N_{\mathrm{Bo}}=0.54$, $p=200$, $n^*=5$; (d) $N_{\mathrm{Bo}}=1.99$, $p=20$, $n^*=8$. The initial configurations for (a)–(d) are slightly noisy circles. The initial configuration for (d) has twofold symmetry, which is broken by roundoff error, illustrating the sensitivity to initial conditions.

The bulbous ends of the labyrinthine branches have a simple explanation. The fluid repels itself, and therefore distributes itself along the labyrinthine arms to maximize the average distance between dipoles (within the restraints imposed by surface tension and area conservation). Therefore the fluid accumulates at the ends of the arms.

The roughly constant arm width can also be understood in terms of statics. The force (4.1) at the edge of a straight arm is dominated by the Biot-Savart force from the opposite side of the arm. This force is outward, and decreases with the arm width. It is countered by the pressure Π induced by area conservation. This pressure is insensitive to small local changes in the arm width (since it is an average of U_0 over the whole system). The width which leads to zero net force on a straight arm will not depend strongly on other details of the structure, and should therefore be roughly constant over the whole labyrinth.

As shown in Fig. 2, at fixed values of p and N_{Bo}, nearly indistinguishable initial conditions lead to quite different labyrinthine structures. (The initial shapes used in most of the calculations shown here were created by adding random amplitudes, uniformly distributed between -0.01 and 0.01, to the 16th through 32nd Fourier modes of the curvature spectrum of a unit circle.) This sensitivity to initial conditions is the result of the effective negative line tension arising from the short-range part of the dipole force. Consider for the moment a system driven by only line tension and area conservation. If the tension is positive, all initial shapes relax to a circle (via the aforementioned curve-shortening equation). Because the

dynamics is first order in time, the model with negative line tension is the time reverse of the model with positive tension. Since all paths in shape space converge if the tension is positive, they must diverge when the tension is negative, implying sensitive dependence on initial conditions. This in turn explains the branching in the experiments and calculations—small bumps on the boundary of the droplet will grow into bigger bumps, which develop into full-fledged arms.

The negative effective line tension arises from the opposition of the fringe field $\mathbf{E}_1$ to the bulk field $\mathbf{E}_0$ near the boundary of the diplar region. When the resulting reduction in the local field energy density compensates for the line tension, it becomes favorable for the system to increase its perimeter. However, because the field energy is not really local, we cannot compute the effective tension exactly. That is, we would like to be able to separate the force integral (4.1) uniquely into long- and short-range parts. The integral could be a sum of two terms, $U_{\rm long}$ and $U_{\rm short}$, with

$$U_{\rm short}(s)\equiv\frac{E_0^2}{8\pi^2}\int_{-\epsilon}^{\epsilon}ds'\hat{\mathbf{R}}\times\hat{\mathbf{t}}'[\sqrt{1+(h/R)^2}-1]\ , \quad (4.11)$$

where ϵ is some suitable cutoff. If $\epsilon\kappa(s)$ is small, then we can approximate the curve in the regime $s-\epsilon\le s'\le s+\epsilon$ by a circular arc with curvature $\kappa(s)$. In this case $R\approx|s|$ and $\hat{\mathbf{R}}\times\hat{\mathbf{t}}'\approx\kappa|s|/2$. Performing the integration, we find that $U_{\rm short}\propto\kappa$ and therefore acts like a line tension. The effective total tension $\tilde{\gamma}$ is $\gamma-U_{\rm short}/\kappa$, or

$$\tilde{\gamma}=\gamma-\frac{E_0^2}{16\pi^2}[\epsilon\sqrt{\epsilon^2+h^2}-\epsilon^2+h^2\sinh^{-1}(\epsilon/h)]\ . \quad (4.12)$$

$\tilde{\gamma}/\gamma$ is a function of the bond number $N_{\rm Bo}$ and the ratio ϵ/h. As in the linear stability analysis in Sec. IV B, we have found that the effective tension can be negative, giving rise to sensitive dependence on initial conditions. Unlike the linear analysis, Eq. (4.12) applies to all shapes. Unfortunately, it does not reduce to an ϵ-independent quantity in any limit, making the definition of $\tilde{\gamma}$ somewhat indeterminate. (The correct choice of the cutoff ϵ may depend on the local geometry, which would lead to a position-dependent effective tension. This would not invalidate any of our conclusions.) For numerical work, where the curve must be discretized, the approximation (4.12) is used with ϵ set to the distance between points on the curve. Without this approximation, an inordinate number of points on the curve would be needed to calculate the integral (4.1) correctly, due to the sharp peak in the integrand at $s=s'$.

At first sight, it is surprising that the initial droplets are not seen to break up into smaller droplets. One would suppose that the true ground state of the system should consist of a number of small droplets, widely spaced to minimize their dipolar interactions, and of a size that minimizes the sum of their dipolar self-energies and surface tension. This is not observed either in the experiments or the numerical dynamics. Vanderlick and Möhwald [16], using a slightly different energy functional, have shown that along certain paths through the space of shapes [namely, the sequences of harmonic shapes

$$\mathbf{r}(\theta)=R_0\frac{1+\eta\cos(n\theta)}{\sqrt{1+\eta^2/2}}\hat{\mathbf{e}}_r(\theta) \quad (4.13)$$

parametrized by an amplitude η and a mode number n] there is a barrier to fission. In other words, the energy functional increases as η in (4.13) goes to unity. For our energy functional we find much the same behavior, except that for some values of the parameters some modes *are* unstable to fission. For example, Fig. 9 shows the total energy as a function of amplitude η for a number of modes. The lowest modes are unstable to fission, but because these are not the most unstable modes of the initial circle, the initial circle (with $\eta=0$) will not move towards the $(n=2,\eta=1)$ separated shape, but rather towards a metastable $(n>2,\eta<1)$ simply connected shape. Although this discussion has been restricted to the unphysical set of shapes given by (4.13), it underscores the necessity of considering dynamics, rather than statics, in describing the labyrinths.

Finally, the relaxation of a branched pattern back to a circle upon the removal of the magnetic field is another important feature seen in experiment [1,12]. Within the present formalism it is described by the curve-shortening dynamics with conserved area, Eqs. (3.14) and (3.15). Since, in the absence of an applied field, the bare energy functional is simply proportional to the length, the dissipative dynamics will drive the length downward in time monotonically until a circular shape is reached. This is illustrated in Fig. 10, for the case of the final state shown in Fig. 2(b). It should be remarked that in experiments one finds that a highly branched pattern will break up into a number of small drops if the magnetic field is suddenly removed. Such topological changes are not contained in our model.

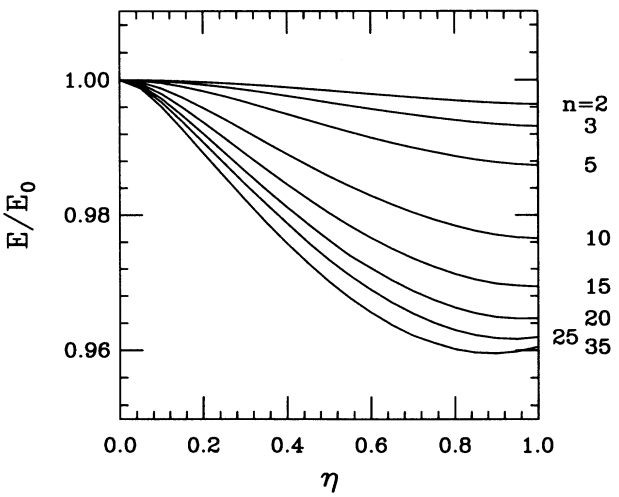

FIG. 9. Energy of the set of variational shapes given by Eq. (4.13), with $N_{\rm Bo}=1.19$ and $p=200$, as a function of the amplitude η for various modes n. The energies are normalized to the energy $\mathcal{E}_0$ of a circle. Modes 2 through 10 are unstable to fission, but will not be attained by the dynamics, which starts at $\eta=0$ and selects mode 35. The global minimum energy is actually $\mathcal{E}/\mathcal{E}_0=0.91$, obtained for $n=104$ widely dispersed droplets.

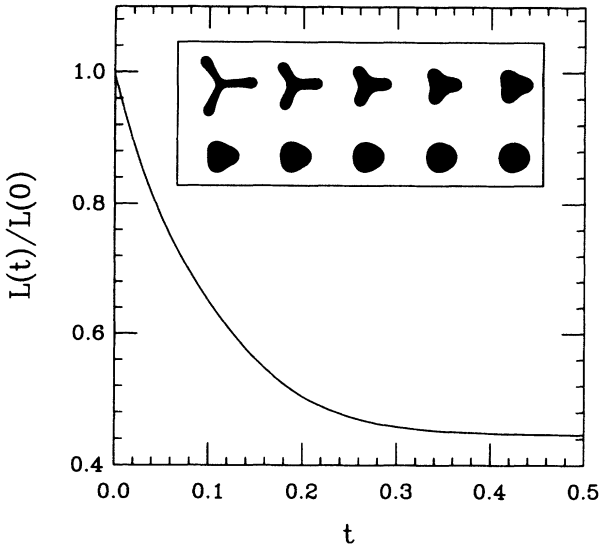

FIG. 10. Relaxation driven by surface tension alone, starting from the final state of Fig. 2(b). The perimeter is also shown as a function of time, demonstrating the monotonicity of the relaxational dynamics.

V. DISCUSSION

The viscous variational dynamics we describe simply moves the system from one configuration to the most energetically favorable neighboring configuration. Treating the system in this way allows us to find the *accessible* labyrinthine configurations. If we had instead searched for true equilibrium states (by solving the functional equation $U[\mathbf{r}(\alpha)]=0$) we would certainly have found kinetically inaccessible configurations—if indeed we had found a solution at all. The success of this simple dynamics in reproducing the observed labyrinths suggests that the pattern formation may be due solely to the structure of the energy functional, and not to complicated hydrodynamic effects. The energy functional has many local metastable minima, corresponding to the many observed labyrinthine patterns, and (perhaps) an inaccessible global minimum. In this sense labyrinth formation is akin to freezing in glasses. It is a dynamic process, because the time evolution cannot be ignored, but it is governed by statics, because the only necessary physical ingredient is the (static) potential-energy functional.

An important unresolved issue is the best means of characterizing the labyrinthine shapes. In particular, it is clear from examination of Figs. 1 and 2 that labyrinths formed in identical environments from nearby initial conditions are similar in certain "coarse-grained" features, such as perimeter and radius of gyration, while still differing in detail. Indeed, the perimeter and radius of gyration exhibit well-defined trends with magnetic field [12]. A quantitative characterization would include some measure of the sensitivity to initial conditions, via a Lyapunov exponent, which would require a suitable definition of the distance between two shapes in configuration space.

As remarked in the Introduction, the purely deterministic motions considered here are directly relevant to macroscopic pattern formation in magnetic fluids. The dynamics of the analogous amphiphilic systems should include thermal fluctuations; the present approach may be viewed as its zero-temperature limit. On a more general level, the related problems of pattern formation and thermal fluctuations of shapes have been studied by other approaches, such a Monte Carlo and molecular-dynamics techniques [26]. The dissipative dynamics used here provides a complementary method for studying such shape evolutions, and can be applied to models of vesicles, biological cells, and polymers [27]. Generalizations to the dynamics of space curves and to two-dimensional surfaces embedded in three dimensions are planned to be considered elsewhere.

ACKNOWLEDGMENTS

We thank our colleagues A. Dickstein and E. Shyamsunder for ongoing collaborations. We are indebted to P. Constantin, N. P. Ong, and M. J. Shelley for important discussions, and to J. Bechhoefer, L. P. Kadanoff, J. S. Langer, J. F. D. Marko, D. M. Petrich, R. Rosensweig, M. Seul, and T. A. Witten for comments. This work was funded in part by National Science Foundation Grant Nos. CHE88-08378, CHE91-06240, the Materials Research Laboratory of the University of Chicago (NSF Grant No. DMR88-19860), and the Natural Sciences and Engineering Research Council of Canada.

APPENDIX: DETAILS OF THE LINEAR STABILITY ANALYSIS

Here we provide some intermediate steps in the derivation of the linear stability relation (4.5). For a linearly perturbed circle, we obtain by straightforward expansions in ζ yield the linearized versions of the various terms in U_0, among them the line element

$$ds \simeq d\varphi(R_0+\zeta) , \tag{A1}$$

curvature

$$\kappa \simeq \frac{1}{R_0}-\frac{1}{R_0^2}\left[\zeta(\varphi)+\frac{\partial^2\zeta}{\partial\varphi^2}\right] , \tag{A2}$$

scalar distance

$$R \simeq 2R_0\left|\sin\left[\frac{\omega}{2}\right]\right|\left\{\frac{1+\zeta(\varphi)+\zeta(\varphi')}{2R_0}\right\} , \tag{A3}$$

cross product

$$\hat{\mathbf{R}}\times\hat{\mathbf{t}}' = \frac{|\csc(\omega/2)|}{2R_0}\left[\zeta(\varphi')-\zeta(\varphi)\cos\omega+\frac{\partial\zeta(\varphi')}{\partial\varphi'}\sin\omega + [2R_0-\zeta(\varphi)-\zeta(\varphi')]\sin^2(\omega/2)\right] , \tag{A4}$$

and potential function

$$\sqrt{1+(h/R)^2} \simeq \frac{\Delta(\omega/2)}{p\,|\sin(\omega/2)|}\left[1-\frac{\zeta(\varphi)+\zeta(\varphi')}{2R_0\Delta^2(\omega/2)}\right] , \tag{A5}$$

where $\omega=\varphi-\varphi'$ and $\Delta(\omega)=\sqrt{1+p^2\sin^2(\omega)}$ and p is defined in (2.8).

Putting this all together, and considering a single excitation of mode number n [i.e., $\zeta(\varphi,t)=\hat{\zeta}_n(t)\cos(n\varphi)$], we may write the growth rate in the form of (4.5) with

$$\mathcal{D}_n(p)=p\int_0^{\pi/2}d\omega(\Delta-p\sin\omega-1/\Delta)+p^2\int_0^{\pi/2}d\omega\left[\frac{\sin^2 n\omega}{\sin\omega}-\frac{p\sin^2 n\omega}{\Delta}\right]. \quad \text{(A6)}$$

Consider the terms in (A6) individually, writing

$$\mathcal{D}_n(p)=p^2[M_n-pL_n(p)]+N(p), \quad \text{(A7)}$$

where

$$M_n=\int_0^{\pi/2}\frac{\sin^2 n\omega}{\sin\omega}d\omega, \quad L_n(p)=\int_0^{\pi/2}\frac{\sin^2 n\omega}{\Delta}d\omega, \quad \text{(A8)}$$

and $N(p)$ is independent of n. The first integral is known (Ref. [28], No. 2.539.4)

$$M_n=\sum_{k=1}^{n}\frac{1}{2k-1}. \quad \text{(A9)}$$

This leaves us with L_n, which is a nontrivial integral. Thiele [5] studied this function and was able to arrive at a systematic expansion in terms of the small parameter $x=1/p^2$. Unfortunately, the coefficients in the expansion are very tedious to calculate for anything but the first two terms.

We will later use an asymptotic approximation which will prove to be very accurate. We first write

$$L_n(p)=\tfrac{1}{2}\int_0^{\pi/2}\frac{1}{\Delta}d\omega-\tfrac{1}{2}\int_0^{\pi/2}\frac{\cos 2n\omega}{\Delta}d\omega \quad \text{(A10)}$$

and combine the first integral with $N(p)$, which becomes

$$\begin{aligned}N(p)&=p\int_0^{\pi/2}\left[\Delta-p\sin\omega-\frac{1}{\Delta}-\frac{p^2}{2\Delta}\right]d\omega\\&=-p^2\int_0^{\pi/2}\sin\omega\,d\omega-\frac{p^2}{2}\int_0^{\pi/2}\frac{p\cos 2\omega}{\Delta}d\omega\\&=-p^2\{1-k^{-1}[E+\tfrac{1}{2}(k^2-2)K]\},\end{aligned}$$

where K and E are complete elliptic integrals of argument k. Combining these results, we obtain the exact final form given in (4.6).

For the special case $n=2$ the integral may be performed analytically by means of the transformation rules for elliptic integrals [28], yielding the critical bond number as a function of the aspect ratio p,

$$N_{bo}^{(2)}=9k(1-k^2)\{k^3+(1-k^2)(8-3k^2)K(k)+(7k^2-8)E(k)\}^{-1}. \quad \text{(A11)}$$

To study the limit of large aspect ratios, we consider values of the mode number n which are small compared to p, or, equivalently, wavelengths large compared to the slab thickness, since $n/p=\pi h/\lambda_n$. The finite sum in (4.6) can be approximated as (Ref. [28], No. 0.132)

$$\sum_{k=1}^{n}\frac{1}{2k-1}\simeq\tfrac{1}{2}\ln(4n\gamma_E)+\mathcal{O}(1/n^2), \quad \text{(A12)}$$

where $\gamma_E=e^C$ with $C\simeq 0.577\,215$ being Euler's constant.

By studying the second integral in (A10) in the limit of large p, one may arrive at the approximation in terms of Bessel functions,

$$\mathcal{D}_n(p)\approx\frac{p^2}{2}[\ln n+K_0(2n/p)-K_0(2/p)]. \quad \text{(A13)}$$

To gain a bit of insight into what this equation means, we exploit the fact that p is generally large, and we are mainly interested in cases where $\lambda>h\Rightarrow n<\pi p$. We expand the Bessel functions and substitute into (A13) to obtain

$$\mathcal{D}_n(p)\simeq\sum_{k=1}^{\infty}\frac{p^{2-2k}}{2(k!)^2}\{(n^{2k}-1)[\psi(k+1)-\ln(n/p)]-\ln n\}, \quad \text{(A14)}$$

where ψ is the psi function. If we now consider values of n small enough so that we only need to keep the first term of the series, then

$$\mathcal{D}_n(p)\simeq\tfrac{1}{2}\{(n^2-1)[1-C-\ln(n/p)]-\ln n\} \quad \text{(A15)}$$

leading to (4.7).

Terms of the form $n^2\ln(n/p)$ originate in the Coulombic nature of the interactions between segments of the boundary in the energy functional (2.5). A simplified heuristic explanation is as follows: For small deviations from a circle, the interactions between the tangent vectors lead to terms in the energy of the form

$$\int d\varphi\int d\varphi'\frac{\partial\zeta(\varphi)}{\partial\varphi}\frac{\partial\zeta(\varphi')}{\partial\varphi'}\Phi\{p|\sin[(\varphi-\varphi')/2]|\}. \quad \text{(A16)}$$

When expressed in terms of the Fourier amplitudes $\hat{\zeta}_n$ such terms give rise to new terms of the form $\sum_n n^2|\hat{\zeta}_n|^2\hat{\Phi}_n$, where $\hat{\Phi}_n$ is the transform of the potential as given in (A16). With a cutoff in the Coulombic behavior in Φ set by the plate spacing h, we readily obtain $\hat{\Phi}_n\sim\ln(n/p)$ and thus the functional form in (4.7).

[1] For a comprehensive treatment of ferrofluids, see R. E. Rosensweig, *Ferrohydrodynamics* (Cambridge University Press, Cambridge, 1985), and references therein.

[2] See, for example, P. A. Rice and H. M. McConnell, Proc. Natl. Acad. Sci. **86**, 6445 (1989).

[3] M. Seul, Physica A **168**, 198 (1990). M. Seul, L. R. Monar, L. O'Gorman, and R. Wolfe, Science **254**, 1616 (1991).

[4] M. Seul and M. J. Sammon, Phys. Rev. Lett. **64**, 1903 (1990).

[5] A. A. Thiele, Bell Syst. Technol. J. **48**, 3287 (1969).

[6] A. O. Tsebers and M. M. Maiorov, Magneothydrodynamics **16**, 21 (1980).

[7] In the parallel-plate geometry of the ferrofluid experiments, the interface motion bears an interesting resemblance to Saffman-Taylor fingering. For a review, see D. Bensimon, L. P. Kadanoff, S. Liang, B. I. Shraiman, and

C. Tang, Rev. Mod. Phys. **58**, 977 (1986).
[8] P. C. Hohenberg and B. I. Halperin, Rev. Mod. Phys. **49**, 435 (1977).
[9] This reduction neglects variations in local magnetization in the ferrofluid and fluctuations in the density in the amphiphile domains.
[10] See, e.g., *Cellular Structures in Instabilities,* edited by J. E. Wesfreid and S. Zaleski (Springer-Verlag, New York, 1984).
[11] See, e.g., J. Bechhoefer, A. J. Simon, A. Libchaber, and P. Oswald, Phys. Rev. A **40**, 2042 (1989).
[12] A. J. Dickstein, R. E. Goldstein, D. P. Jackson, S. A. Langer, and E. Shyamsunder (unpublished).
[13] D. J. Keller, J. P. Korb, and H. McConnell, J. Phys. Chem. **91**, 6417 (1987).
[14] In principle, the divergence theorem applies only if the quantity $\mathbf{A}\times\mathbf{E}_1$ has no singularities on internal boundaries. It is not obvious *a priori* that there are no singularities on the boundary of the slab. Tediously rederiving (2.5) without using the divergence theorem shows that the theorem is indeed applicable. In [13] the small h approximation was made by dropping the z integration in (2.2). In this case the divergence theorem does not apply, unless additional short-distance cutoffs are introduced.
[15] H. M. McConnell and V. T. Moy, J. Phys. Chem. **92**, 4520 (1988).
[16] T. K. Vanderlick and H. Möhwald, J. Phys. Chem. **94**, 886 (1990).
[17] L. Lorenz, Wied. Ann. **7**, 161 (1879).
[18] H. Goldstein, *Classical Mechanics* (Addison-Wesley, Reading, 1980), p. 24.
[19] S. F. Edwards and K. F. Freed, J. Chem. Phys. **61**, 1189 (1974).
[20] Equation (3.2) is the simplest term one might expect from a rigorous calculation of the dissipation function. A complete calculation would include viscous dissipation at all points inside and outside the contour, and possibly the effects of eddy currents due to the changing shape.
[21] M. Doi and S. F. Edwards, *The Theory of Polymer Dynamics* (Oxford University Press, New York, 1986).
[22] The two-dimensional cross product, $\mathbf{a}\times\mathbf{b}\equiv\epsilon_{ij}a_i b_j$ is a scalar.
[23] J. S. Langer, in *Chance and Matter, Les Houches Session XLVI, 1986,* edited by J. Souletie, J. Vannimenus, and R. Stora (Elsevier, New York, 1987), and references therein; R. C. Brower, D. A. Kessler, J. Koplik, and H. Levine, Phys. Rev. A **29**, 1335 (1984); P. Constantin (private communication).
[24] See, e.g., M. E. Gage, Invent. Math. **76**, 357 (1984); U. Abresch and J. Langer, J. Diff. Geom. **23**, 175 (1986); M. Gage and R. S. Hamilton, *ibid.* **23**, 69 (1986), and references therein.
[25] Aspects of this analysis have been discussed previously; see Ref. [6].
[26] See, e.g., *Statistical Mechanics of Membranes and Surfaces,* Proceedings of the Jerusalem Winter School for Theoretical Physics, Vol. 5, edited by D. Nelson, T. Piran, and S. Weinberg (World Scientific, Singapore, 1989).
[27] R. E. Goldstein and S. A. Langer (unpublished).
[28] I. S. Gradshteyn and I. M. Ryzhik, *Tables of Integrals, Series, and Products* (Academic, New York, 1980).